

Dominant Balances and Exchanges of the Atmospheric Water Cycle in the Reanalysis 2 at Diurnal, Annual, and Intraseasonal Time Scales

ALEX C. RUANE AND JOHN O. ROADS

Experimental Climate Prediction Center, Scripps Institution of Oceanography, University of California, San Diego, La Jolla, California

(Manuscript received 30 April 2007, in final form 28 June 2007)

ABSTRACT

Output from the National Centers for Environmental Prediction–Department of Energy (NCEP–DOE) Reanalysis 2 (R2) is passed through a broadband filter to determine the normalized covariances that describe the variance of the atmospheric water cycle at diurnal, annual, and intraseasonal (~ 7 –80 days) time scales. Vapor flux convergence is residually defined to close the water cycle between successive 3-hourly output times from 2002 to 2004, resulting in a balance between precipitation, evaporation, precipitable water tendency, and vertically integrated vapor flux convergence. The same balance holds at each time scale, allowing 100% of each variable's temporal variance to be described by its covariance with other water cycle components in the same variance category. Global maps of these normalized covariances are presented to demonstrate the unique balances and exchanges that govern temporal variations in the water cycle.

The diurnal water cycle is found to be dominated by a land–sea contrast, with continents controlled thermodynamically through evaporation and the oceans following dynamic convergence. The annual time-scale features significant meridional structure, with the low latitudes described mostly through variability in convergence and the extratropics governed by the properties of advected continental and maritime air masses. Intraseasonal transients lack direct solar oscillations at the top of the atmosphere and are characterized by propagating dynamic systems that act to adjust the precipitable water content of unsaturated regions or exchange directly with precipitation in saturated areas.

By substituting the modeled precipitation with observation-based fields, a detailed description of the water cycle's exchanges relating to the nocturnal precipitation maximum over the Midwest is obtained.

1. Introduction

Nearly all atmospheric activity is originally derived from external solar forcing. On time scales of a year and less, this forcing arrives in the form of a strong daily signal resulting from the rotation of the earth and a seasonal signal due to the earth's orbit and inclination. The diurnal and annual cycles of solar insolation are therefore fundamental to the earth's water cycle, but do not necessarily drive an equivalent response. Energy from these solar forcings interacts with the earth system to excite other time scales, leading to many possible regimes in the water cycle's behavior.

Examinations of the water cycle have been conducted on seasonal (e.g., Roads and Betts 2000; Roads et al. 2002) and diurnal (e.g., Anderson and Kanamaru

2005; Lee et al. 2007) time scales. Ruane and Roads (2007a, hereafter RR07a) examined the atmospheric water cycle's diurnal phase and amplitude over North America as part of an investigation into the water and energy cycles of reanalysis models, finding that parameterization errors propagate throughout the system. In particular, the convective parameterizations employed by global reanalyses were found to have a quick trigger that initiated weak convection in the afternoons over land despite the proper supply of moisture for the more diverse observed precipitation maxima.

Ruane and Roads (2007b, hereafter RR07b) analyzed the variance distribution of five global precipitation sets at high temporal and spatial resolution, identifying significant regions of activity across many variance categories between 6-h and 1-yr periods. In addition to a considerable land–sea contrast, signatures of the Hadley circulation, major monsoons, diurnal circulations, and the Madden–Julian oscillation (MJO; Madden and Julian 1994) were present in the three

Corresponding author address: Alex Ruane, University of California, San Diego, #0224, La Jolla, CA 92093.
E-mail: aruane@ucsd.edu

satellite-derived precipitation products and the two reanalysis models. To further explore the role of these and other features in the water cycle, this study complements RR07b by analyzing the variance of balanced water cycle components; isolating unique water cycle mechanisms in many regions of the globe. The results may be used to diagnose model biases or to isolate the underlying water cycle behaviors that cause diverse regional hydroclimates.

Section 2 introduces the reanalysis modeling system and methodologies employed in this study, including a comparison between model spinup and natural precipitable water tendency. Section 3 describes the variance of each water cycle variable through its normalized covariance with the other components of the water cycle at diurnal, annual, and intraseasonal time scales. This process is repeated in section 4 utilizing a satellite-derived precipitation product to replace modeled precipitation, followed by brief conclusions in section 5.

2. Datasets and methodologies

a. The NCEP–DOE Reanalysis 2 model

Simulations of the National Centers for Environmental Prediction–Department of Energy (NCEP–DOE) Reanalysis 2 model (R2; Kanamitsu et al. 2002b) are the basis of this study. The R2 is a global spectral model utilizing a primitive equations system of virtual temperature, humidity, surface pressure, momentum prognostic equations, and various physical parameterizations (for land surface processes, precipitation, radiation, etc.). Precipitation and evaporation are put out on a 192×94 Gaussian grid (each pixel $\sim 1.9^\circ$ across), but the model uses 62 spherical harmonics with a triangular truncation and 28σ levels (T62L28). Vertically integrated variables (e.g., precipitable water) are calculated from their comprehensive model values to prevent interpolation errors.

The model output examined here covers 2002–04 and was generated as part of the Experimental Climate Prediction Center's contribution to the Coordinated Enhanced Observing Period (CEOP; Koike 2004; Lawford et al. 2006). This time period also facilitates comparisons with the precipitation sets examined in RR07b. Augmented 6-h forecasts were initialized from reanalyzed observations 4 times each day (at 0000, 0600, 1200, and 1800 UTC), and successive 3- and 6-h forecasts link together to form a comprehensive time series. Each forecast time represents the 3-h period preceding it from the same initialization, so a 6-h forecast of precipitation represents the mean precipitation rate between 3 and 6 h of model time, for example. As precipitation and evaporation are not assimilated, these

short model forecasts are required to simulate the water cycle's evolution from the assimilated atmospheric states.

Notable parameterizations employed by the R2 include the Simplified Arakawa–Schubert convection scheme (SAS; Pan and Wu 1995) and the Oregon State University land surface model (OSU2; Pan and Mahrt 1987). To prevent runaway soil moisture values, adjustments in the reanalysis are made according to biases between simulated and observed precipitation over each 5-day pentad (see Lu et al. 2005, for a full description). The model's atmosphere is forced by weekly mean sea surface temperatures (SSTs) that are linearly interpolated into mean daily values, resulting in diurnally constant SSTs. This assumption stems from the fact that the open-ocean surface's large heat capacity drastically diminishes the daily range of surface temperature compared to land. Diurnally constant SSTs therefore have only a small impact on the diurnal magnitude of turbulent energy fluxes, but the phases are strongly affected (RR07a).

b. Water cycle balance

At any given time, the total amount of water vapor in the atmospheric column is represented by the precipitable water:

$$w = \int_0^1 \pi q d\sigma, \quad (1)$$

where q is the specific humidity and π represents the atmospheric mass, which is the surface pressure divided by gravity: $\pi = p_s/g$. The tendency of precipitable water between successive model output times may be calculated via

$$T = \frac{1}{t - t_0} \int_{t_0}^t \frac{\partial w}{\partial t} dt. \quad (2)$$

Precipitable water tendency has both a natural and a model component, the latter a result of model biases, spinup, and reinitializing the atmospheric state every 6 h. These dual-tendency components may be separated by comparing overlapping forecasts from successive initializations, and are discussed in more detail in section 2e.

While vertical vapor fluxes do not change precipitable water content, the precipitable water amount does change due to horizontal convergence of vapor flux, given by

$$C = - \int_0^1 (\nabla \cdot \pi q \nabla) d\sigma. \quad (3)$$

Atmospheric moisture may also be added through evaporation (E) from the surface or lost to precipita-

tion (P) that falls out of the column. Together, the exchanges of the water cycle may be balanced by

$$T = C + E - P. \quad (4)$$

In short, any exchange of moisture through one of these four processes must be balanced by changes in the others. Vapor convergence and evaporation add moisture to the column, leading to either a positive moisture tendency or a corresponding loss of moisture through precipitation. Dominant balances occur when two terms dwarf the other two components of the water cycle, while dominant exchanges exist when moisture is commonly interchanged between two components in a given region, regardless of their magnitude.

The output of the R2 allows exact accounting for the T , E , and P terms of this balance in principle, but puts out only instantaneous values of C . Interpolations of these instantaneous values do not correctly represent the variation of horizontal vapor fluxes over a 3-h period, so vapor flux convergences in this study were residually calculated ($C = T - E + P$) to perfectly close this balance for every forecast time. A similar residual vapor flux convergence closure compared favorably with comprehensive output over North America in RR07a, where it even captured the nocturnal maximum seen over the upper midwestern United States.

The T is derived from assimilated observations, but each term on the right-hand side of Eq. (4) is driven by a different mechanism in the R2. The C is determined by dynamic activity throughout the atmospheric column, although changes in motion in the moist lower troposphere generally have the greatest influence on the water cycle. The E is a function of the atmospheric boundary layer's thermodynamic influence on evaporative parameterizations, and is therefore strongly affected by radiative forcings (see, e.g., RR07a). The P is heavily parameterized in the R2, and is therefore dominated by the triggering mechanisms and dynamic algorithms hard-wired into the SAS convection scheme, although boundary layer and other parameterizations also feed into the environmental conditions that drive convection. Like the other convection schemes noted by Trenberth et al. (2003), SAS convective precipitation is too light and initiates prematurely over many land areas.

Each term in Eq. (4) may also be considered as a sum of its mean (denoted with an overbar) and transient (denoted by a prime) components:

$$(\bar{T} + T') = (\bar{C} + C') + (\bar{E} + E') - (\bar{P} + P'). \quad (5)$$

The atmospheric water balance therefore holds over both the long-term mean and among the transients at any orthogonal frequency:

$$\bar{T} = \bar{C} + \bar{E} - \bar{P}, \quad (6a)$$

$$T' = C' + E' - P'. \quad (6b)$$

c. Mean water cycle balance

Following Eq. (6a), the mean of each water cycle component over the 2002–04 period is shown in Fig. 1. As expected, \bar{P} is strongest in the intertropical convergence zone (ITCZ) and over the Indonesian warm pool. The storm-track regions just downwind of the Kuroshio and Gulf Stream also appear as local maxima. The \bar{E} is strongest over these western boundary currents as well as where large-scale subsidence from the Hadley circulation provides hot and dry air over warm subtropical oceans. Moist and arid continental regions also have noticeable differences in \bar{E} . The residually defined \bar{C} identifies a pattern of divergence from the high-evaporation regions over the subtropical oceans and convergence in the ITCZ. Weak net convergence is also apparent in the storm-track areas over the mid- and high-latitude oceans. Over long time periods the precipitable water tendency is expected to be negligible, as accumulated vapor flux convergence, evaporation, and precipitation are far greater than their net impact on the reservoir term. The \bar{T} is the smallest term in the mean balance, but its nonnegligible values indicate the importance of model tendencies; these are discussed further in section 2e.

d. Transient water cycle balance

Global maps of the transient balances of the water cycle [Eq. (6b)] for the diurnal, annual, and intraseasonal time scales were generated in a four-step procedure. First, time series of the deviation from the annual mean of each component of the water cycle were generated at each grid point (see, e.g., Fig. 2a).

Second, each component's series were bandpass-filtered using a fast Fourier transform (Emery and Thomson 2004) that casts each component into frequency space and isolates orthogonal frequencies in the three variance categories shown in Fig. 2b. The annual category contains variance with periods between ~ 80 and ~ 365 days, containing seasonal shifts such as the monsoons and the migration of the ITCZ. The intraseasonal category captures variance between ~ 7 and ~ 80 days, which is independent from direct solar forcing oscillations at the top of the atmosphere and includes the frequencies associated with the MJO and many propagating synoptic systems. Variance categories between 6 h and 7 days, with the exception of the exact diurnal frequencies, were not examined here.

Our definition of the diurnal category is based upon the spectral signature of diurnal solar forcing (Fig. 2c).

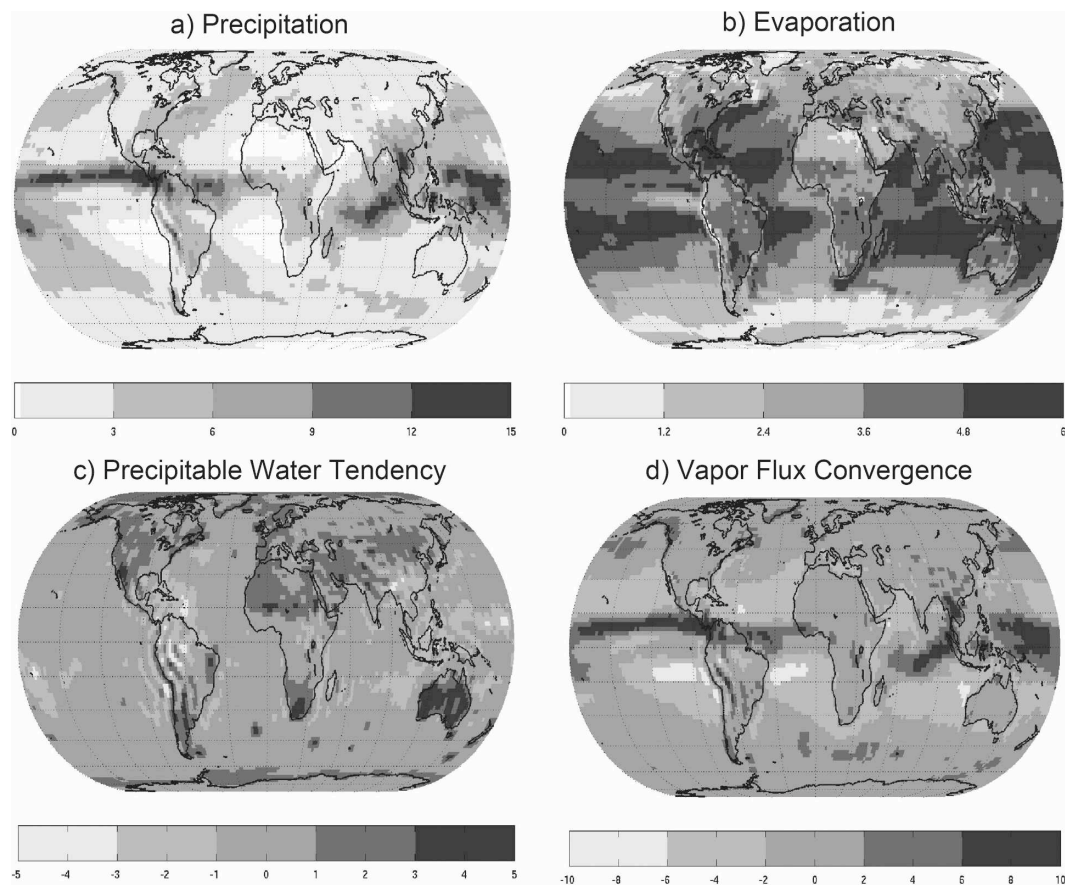


FIG. 1. The 2002–04 water cycle component means (mm day^{-1}): (a) precipitation, (b) evaporation, (c) precipitable water tendency, and (d) vapor flux convergence.

The sharp peaks generated by the solar radiation correspond to the 4 harmonics (with 24-, 12-, 8-, and 6-h periods) that are needed to capture the mean diurnal cycle at 3-hourly resolution, but the mean diurnal cycle is not repeated consistently every day. Over a full year, many slightly different daily realizations broaden the spectral peaks, so the diurnal variance category is defined to capture at least 98% of the variance of each of these sharp solar forcings in narrow bands that contain three frequencies centered upon each diurnal peak. Figure 2d shows the bandpass-filtered diurnal, annual, and intraseasonal variance categories for 2002 precipitation for the grid point that contains Lindenberg, Germany. By capturing slightly offsetting frequencies around these diurnal peaks, a longer time scale is aliased that retains seasonal adjustments in the magnitude of the diurnal variation. For example, the narrow bands that define the diurnal variance category capture a seasonal adjustment in the diurnal range of incoming solar radiation (not shown), reaching a maximum at the summer solstice (Julian day 172) and a minimum near

the winter solstice (Julian day 355). The annual and diurnal categories both show an increase in magnitude during the warmest portion of the year when continental convection is at its maximum. The lowest diurnal range occurs in the late winter (near Julian day 70), when convection is at a minimum. These variance categories are similar to those used in RR07b, but the intraseasonal band is expanded.

Third, after the components have been bandpass filtered and cast back into a 3-hourly time series, the variance of each component:

$$\text{var}(A') = \frac{1}{N-1} \sum_1^N (A')^2, \quad (7)$$

as well as the covariance between the various components:

$$\text{cov}(A', B') = \frac{1}{N-1} \sum_1^N A' B' \quad (8)$$

is calculated for every grid point each year.

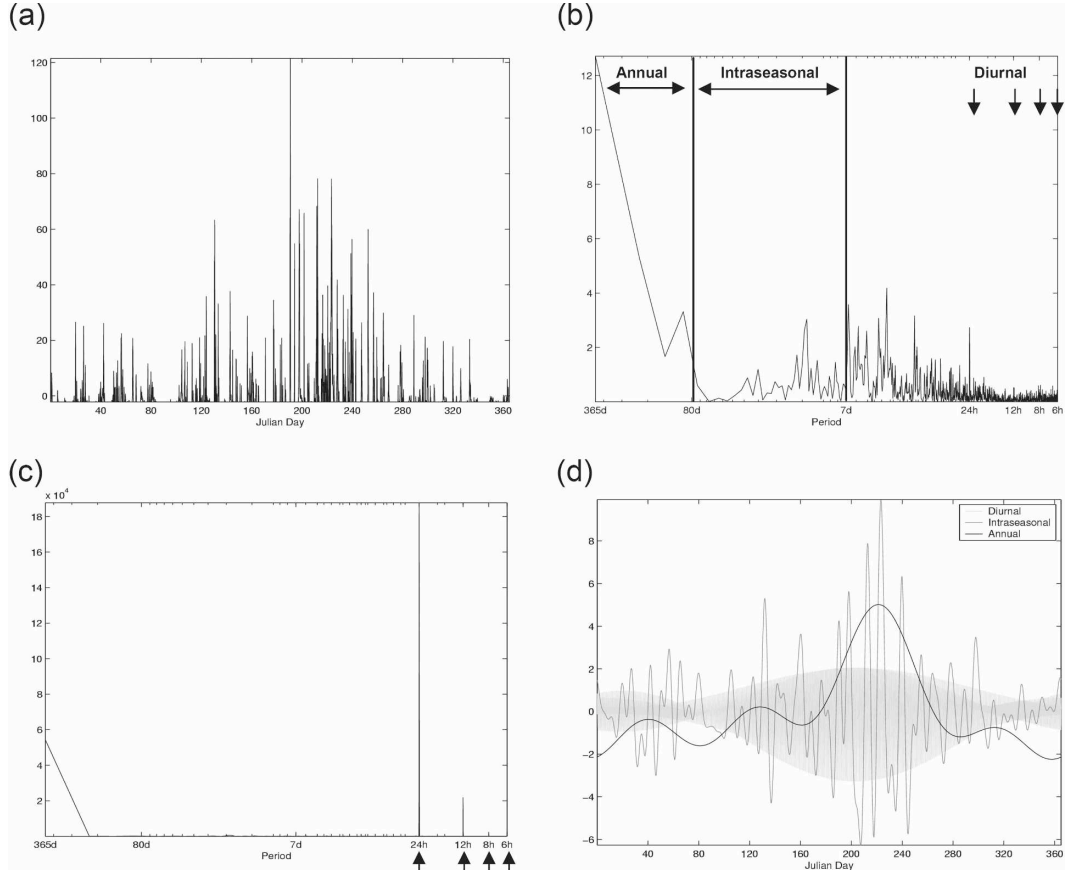


FIG. 2. Methodology example for Lindenberg, Germany, in 2002: (a) 3-hourly precipitation rate (mm day^{-1} ; deviation from the mean); (b) variance spectrum of precipitation rate [$(\text{mm day}^{-1})^2$; with variance category definitions]; (c) variance spectrum of surface downward shortwave radiation flux [$(\text{W m}^{-2})^2$ with four diurnally forced peaks]; and (d) bandpass-filtered time series of precipitation for each variance category (mm day^{-1}). The diurnal category oscillates so rapidly that it appears to blend together into the shaded envelope here.

Equation (6b) indicates that any deviation in one component of the water cycle must be matched by change in other components. This balance may be extended into variance by calculating the covariance of each term in the equation to a particular variable, then normalizing by the variance of that variable. As an ex-

ample, for the tendency term, this is equivalent to multiplying each n th member of the bandpass-filtered time series in Eq. (6b) by $T'_n/\Sigma(T')^2$ and then performing a summation over all n . With some rearrangement, and bringing negative signs inside the covariance to enable a convenient sum between terms, we have the following:

$$\frac{\text{cov}(P', P')}{\text{var}(P')} \times 100\% = \frac{\text{cov}(E', P') + \text{cov}(-T', P') + \text{cov}(C', P')}{\text{var}(P')} \times 100\% = 100\%, \quad (9a)$$

$$\frac{\text{cov}(E', E')}{\text{var}(E')} \times 100\% = \frac{\text{cov}(P', E') + \text{cov}(T', E') + \text{cov}(-C', E')}{\text{var}(E')} \times 100\% = 100\%, \quad (9b)$$

$$\frac{\text{cov}(T', T')}{\text{var}(T')} \times 100\% = \frac{\text{cov}(-P', T') + \text{cov}(E', T') + \text{cov}(C', T')}{\text{var}(T')} \times 100\% = 100\%, \quad (9c)$$

and

$$\frac{\text{cov}(C', C')}{\text{var}(C')} \times 100\% = \frac{\text{cov}(P', C') + \text{cov}(-E', C') + \text{cov}(T', C')}{\text{var}(C')} \times 100\% = 100\%. \quad (9d)$$

These “normalized covariances” indicate the portion of one component’s variance that is matched by another. As an example, the first term in the center portion of Eq. (9a) indicates the percentage of precipitation’s variance that corresponds to variance of evaporation. Although covariance is commutative, $\text{cov}(A', B') = \text{cov}(B', A')$, the terms in the center portion of Eqs. (9a–d) are not commutative because they are normalized by a single component’s variance, although complementary terms will always have the same sign.

Each of these normalized covariance terms indicates a potential dominant balance or exchange in the atmospheric water cycle. For example, if there was no change in precipitable water tendency or vapor convergence, any increase in evaporation must be matched with precipitation. If there was no variation in evaporation or vapor convergence, any precipitation event must be removing moisture from the column, causing a negative tendency in precipitable water. If precipitation and the tendency term were held constant, evaporation into the column must be matched by an equal vapor flux divergence.

Finally, maps of these normalized covariances [Eqs. (9a–d)] are produced by averaging the normalized covariant percentages at each grid point over the three annual segments in each variance category. As each component’s variance may be explained by its normalized covariance with the other three components of the water cycle, the sum of these three maps are exactly 100% at every grid point. If the percentage normalized covariance between two components in a given variance category ranges more than 100% between years over a particular grid point, it is omitted for displaying too much uncertainty in its interannual variation (white portions of the figures). The strength of this method is its ability to confidently explain the comprehensive variation of a component’s deviations in a particular variance category, so if uncertainty exists in any normalized covariant term the grid point is omitted in all other terms of the same balance. These maps [representing Eqs. (9a–d)] form the primary bases for examinations in this study.

Heeding the warnings by Randall et al. (1991), it is both tempting and incorrect to use the normalized covariances to fully delineate the cause of particular patterns. These maps really indicate coincident behaviors; a determination of which component caused the changes in the other components requires additional analysis and physical insight, which is provided in section 3 for select features. This procedure will underemphasize lagged responses in the atmosphere, as differences in phase will appear only as a reduction in the magnitude of the simultaneous normalized covariance.

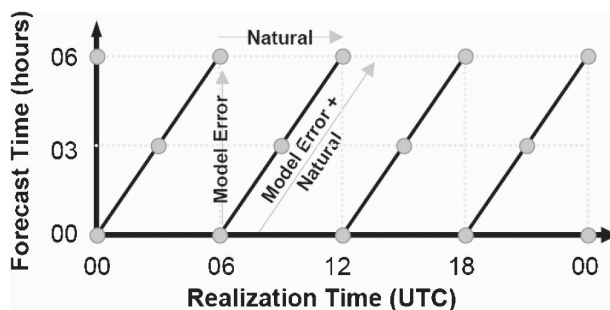


FIG. 3. Experiment design overview. Each diagonal line represents a continuous simulation and each circle represents an output time. The gray arrows indicate the differences that separate the model error and natural precipitable water tendencies.

e. Model versus natural tendencies

A water cycle imbalance due to model error tendency [introduced by successive reinitializations of the NCEP–National Center for Atmospheric Research (NCAR) reanalysis] has been identified by a number of authors, including Trenberth and Guillemot (1995, 1998). In contrast to their work (which also used a residual technique to compute an $E - P$ term at monthly and longer time scales) precipitable water tendency is computed here at much shorter 3-hourly intervals [Eq. (2)], where the budget is balanced. Although the natural precipitable water tendency is negligible on long time scales, Randall et al. (1991) recognized that the tendency term may be significant on shorter time scales. RR07a also noted a significant diurnal tendency component over North America in three different reanalysis systems due in part to convective parameterization errors. To fully understand the implications of the normalized covariances in sections 3 and 4, it is important to determine whether the tendency variations are due to its model or natural components.

The format of the reanalysis experiment allows for a clear separation of these two components on 6-hourly time scales due to an overlap of the instantaneous 6-h precipitable water forecast and the analysis field of the next initialization (see Fig. 3). These dual, coincident states may be compared to the precipitable water field 6 h later to provide insights into model and natural behavior. As noted above, the evolution of precipitable water from its analysis field to a 6-h forecast contains both model error (ET) and natural (NT) tendencies:

$$T = ET + NT = \frac{w_{06,06} - w_{06,00}}{0.25 \text{ day}}, \quad (10)$$

where $w_{06,00}$ indicates the 0-h forecast (analysis) of precipitable water from a 0600 UTC initialization. The tendency between the 6-h forecast and the previous 6-h

forecast is indicative of the natural processes according to the model's assimilation system:

$$NT = \frac{w_{06,06} - w_{00,06}}{0.25 \text{ day}}. \quad (11)$$

The model error tendency may therefore be estimated by subtracting the natural tendency from the total tendency over a 6-h forecast period:

$$ET = T - NT = \frac{w_{00,06} - w_{06,00}}{0.25 \text{ day}}. \quad (12)$$

To understand the role of these two tendency terms, analysis of the 6-hourly time series from 2002–04 was conducted in a corresponding manner to the methodology in section 2 (not shown). Here \overline{NT} is less than 0.1 mm day^{-1} across the entire globe, more than 50 times smaller than \overline{ET} , which is nearly identical to the \overline{T} shown in Fig. 1c. In addition to large biases over arid regions, wave patterns in and around major mountain ranges suggest the influence of a topographical mechanism in model error tendency. The variance of NT' exceeds the variance of ET' in the diurnal and intraseasonal category, although the variance of ET' is much larger in the annual category. Regions with dense upper-air measurements show particularly strong ET' variance, as do island rawinsonde stations (forming bull's-eyes similar to those seen by Trenberth and Guillemot 1998).

The T' terms shown in the following sections contain both ET' and NT' , but several patterns emerged from analysis of the 6-h separated model error and natural tendency transients (not shown). On the diurnal time scale (section 3a), patterns relating to T' are overwhelmingly due to NT' . Intriguingly, however, ET' acts to reduce regional anomalies in the covariance of T' and E' . On the annual time scale (section 3b), NT' is negligible, so patterns in T' match ET' . On intraseasonal time scales (section 3c), the T' variance is small and mostly explained by NT' , although ET' makes a significant contribution to T' over land.

3. Transient behavior of the water cycle

Maps of the normalized covariances of various water cycle components are shown in this section for diurnal (Fig. 4), annual (Fig. 5), and intraseasonal (Fig. 6) time scales. These maps are displayed in sets of 3s to enable the full depiction of a particular variable through its normalized covariance with the other three components. For example, Figs. 4a–c describes 100% of the daily variance of P' at all points on the globe. Figure 4a examines the normalized covariance of evaporation to

precipitation; equivalent to the $\text{cov}(E', P')/\text{var}(P')$ term in Eq. (9a). The other two maps in the first row correspond to the next two terms in this equation. A grid point showing a normalized covariance of 100% in Fig. 4a indicates that the variance of E' accounts for the entire variance of P' . A grid point showing 0% indicates no relationship between the variations of the two variables. A grid point showing <0% indicates that E' and P' covary, but with an opposite phase. A grid point displaying a normalized covariance >100% has E' and P' covarying in approximate phase, but with E' displaying a larger magnitude than P' . It should also be noted again that, because of the differing normalizations, the normalized covariance of evaporation to precipitation (Fig. 4a) is different than the normalized covariance of precipitation to evaporation (Fig. 4d).

a. Diurnal variance description

Normalized covariances of the water cycle components' diurnal variability are shown in Fig. 4. It is immediately apparent that there is a strong land–sea contrast in nearly all of the diurnal components. The land surface's low heat capacity leads to strong diurnal variations, but the R2 may overly diminish diurnal variations over the oceans because of diurnally constant SSTs (as discussed in section 2a). The constant thermodynamic state over the oceans leads to low diurnal evaporation variance over the oceans, providing a negligible denominator that leads to a wide interannual range in normalized covariances in Figs. 4d–f. As a result, the dynamic vapor flux convergence component drives most variance in the water cycle over the oceans at this time scale (Figs. 4c,i). Over the ocean, precipitation also receives a small portion of its moisture through an erosion of the precipitable water reservoir (Fig. 4b).

The normalized covariances that describe the variance of precipitation (Figs. 4a–c) are insignificant over arid and stratocumulus regions where large-scale subsidence inhibits precipitation. It is not surprising to see strong covarying E' and P' over land (see, e.g., Anderson et al. 2008). As the incoming solar radiation reaches its peak at midday, surface temperatures rise rapidly and evaporation peaks shortly thereafter. The evaporated moisture increases lower-tropospheric moisture availability and promotes afternoon convection in the destabilizing atmospheric column. The normalized covariance of E' to P' demonstrates that evaporation displays much more variance than the less-consistent precipitation over the Northern Hemisphere continents (more than twice as much in many places), but the two components have a similar phase. This imbalance is remedied by a seemingly counterintuitive diurnal rela-

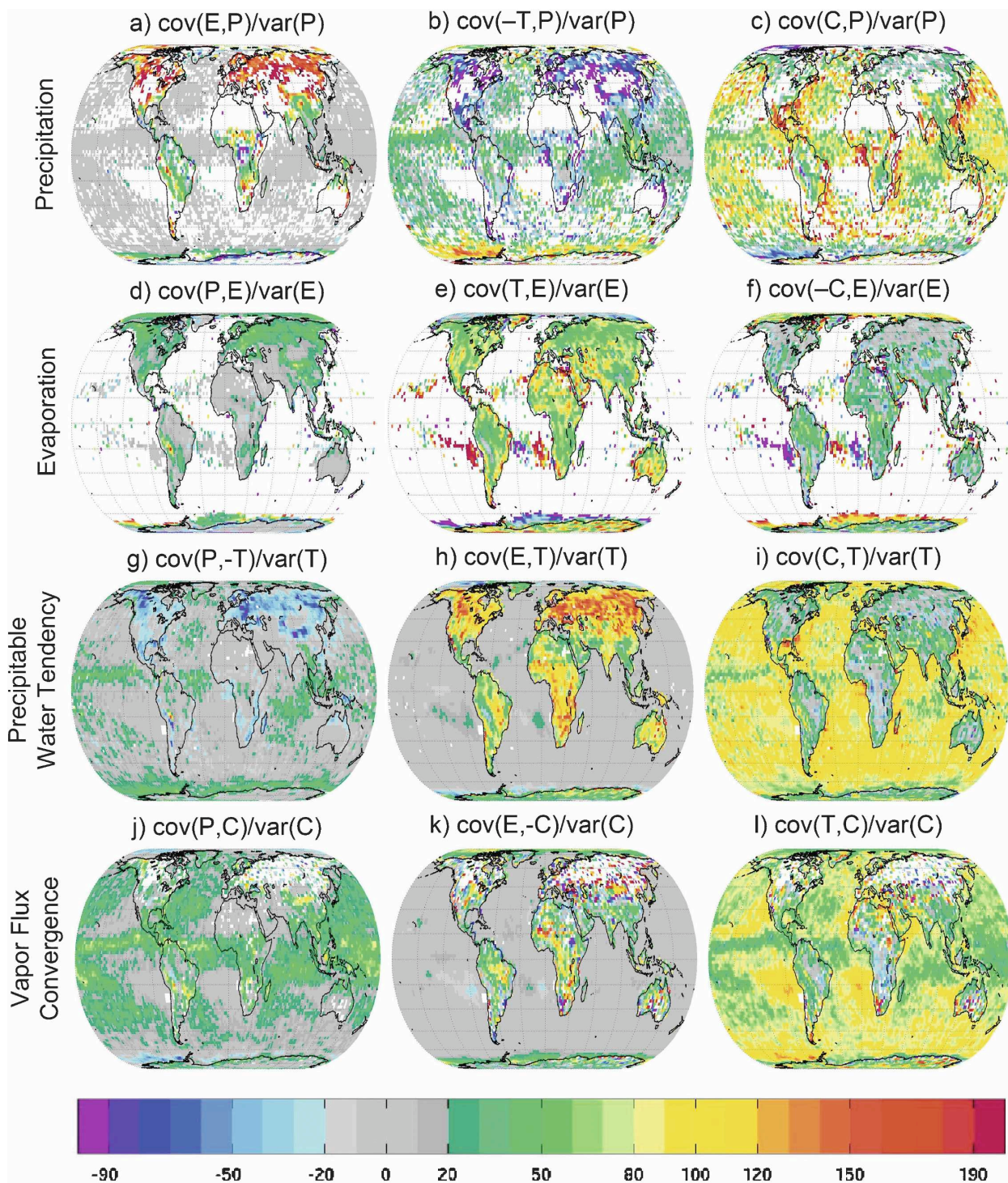


FIG. 4. Diurnal normalized covariance maps describing diurnal variance (%) from 2002 to 2004 in the R2. The sum of each row describes 100% of the diurnal variance of the component listed at left by its normalized covariance with the other components: (a)–(c) the three terms in the center of Eq. (9a); (d)–(f) represent the terms in Eq. (9b); (g)–(i) represent the terms in Eq. (9c); and (j)–(l) represent the terms in Eq. (9d). White grid points represent locations where the variance description was insignificant.

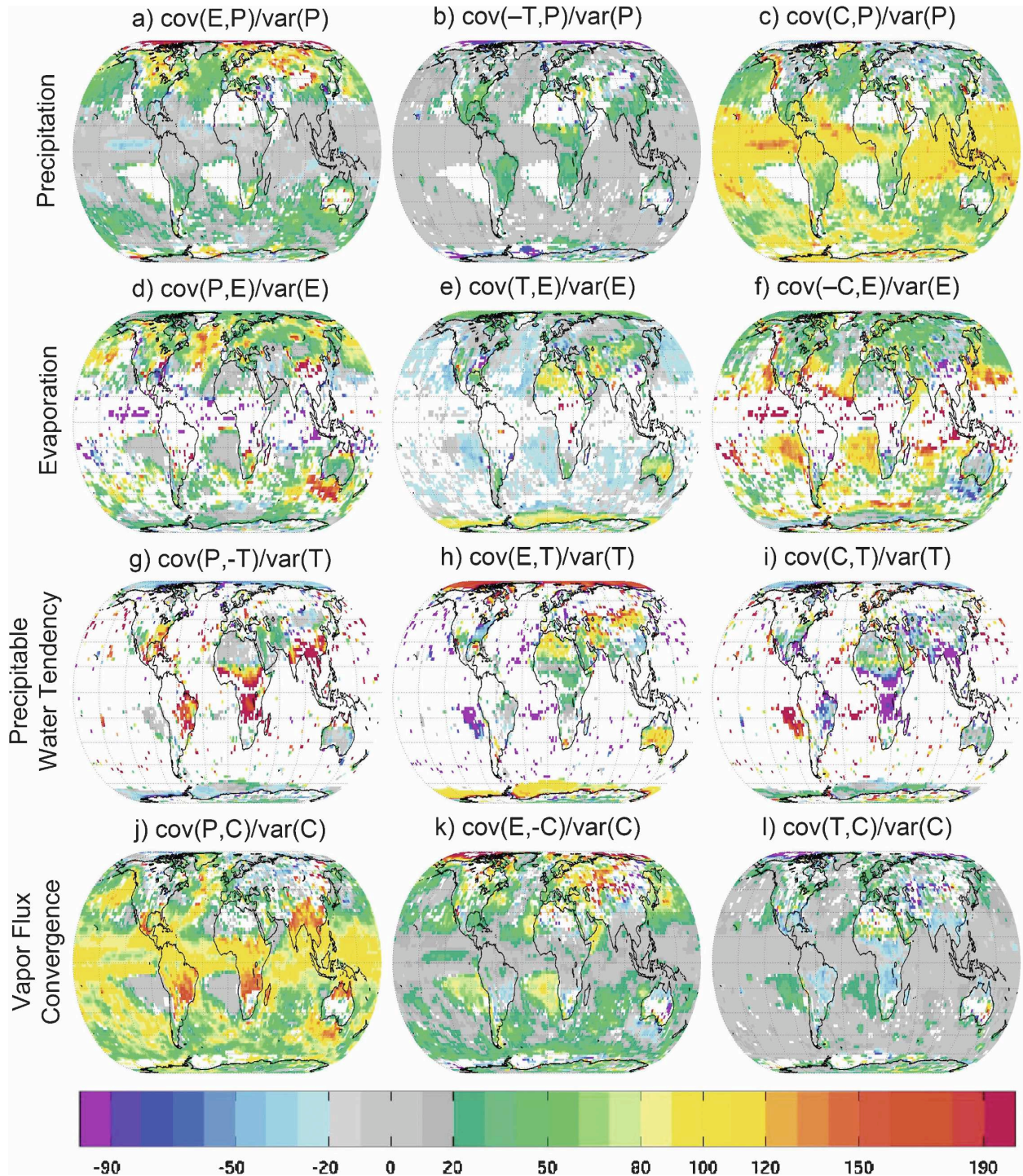


FIG. 5. As in Fig. 4, but for annual variance.

tionship between P' and T' , where diurnal precipitation variability seems to be in phase with gains in the water column. Of course precipitation events do not add more moisture into the atmosphere, but this feature is a result of a conglomeration of many daily realizations

that display fundamentally different traits. Although infrequent convective events are large, the regular evaporative signal dominates the diurnal variability of precipitable water tendency over any given year despite its relatively small diurnal amplitude. Therefore, P' and T'

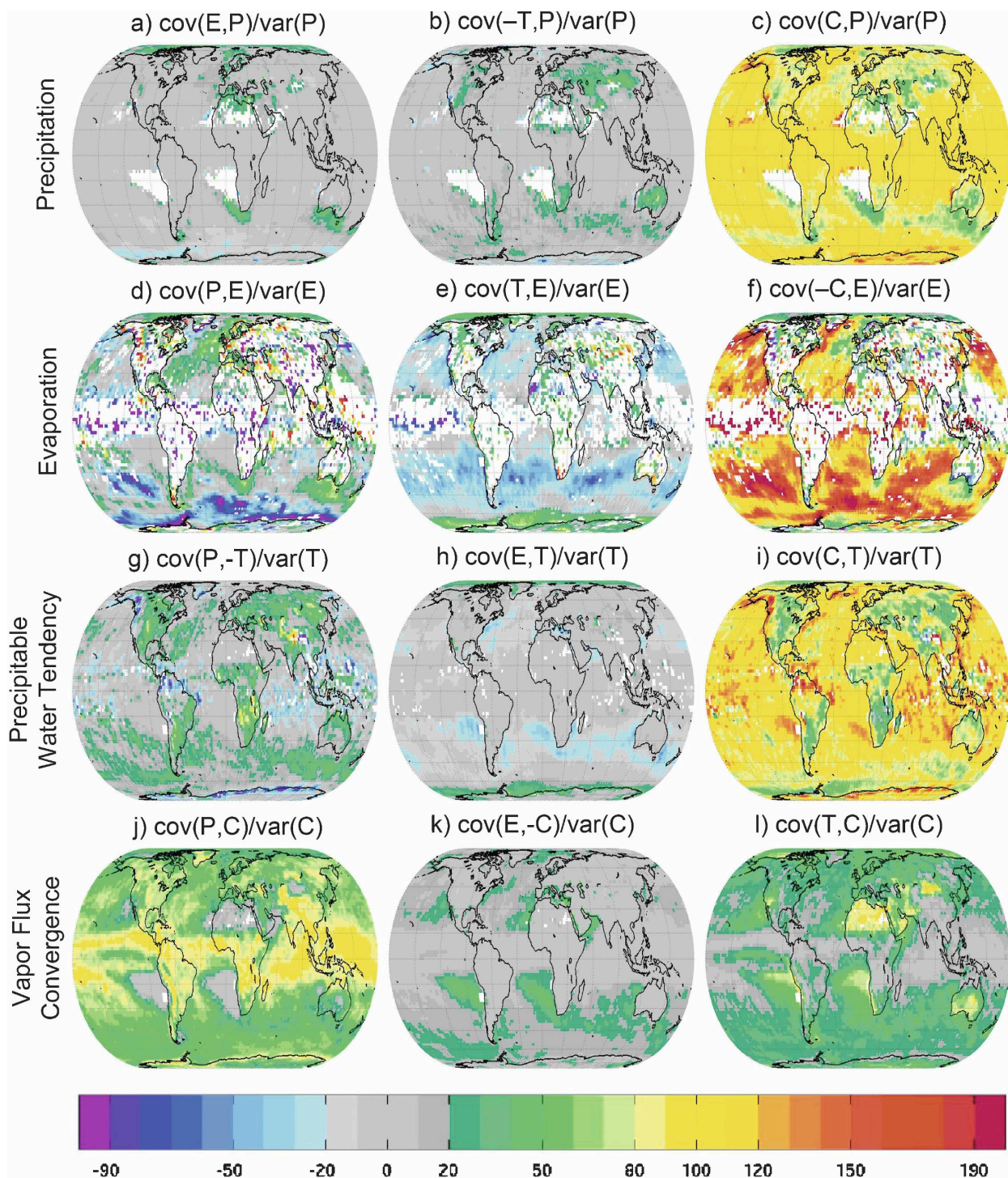


FIG. 6. As in Fig. 4, but for intraseasonal variance.

share the same diurnal phase even if they do not occur on the same days.

The normalized covariance description of T' variance in Figs. 4g–i reinforces this explanation and displays the clear contrast between the thermodynamic control of

the continents' water cycle and the dynamic control of the oceans' water cycle. As mentioned in the previous section, the variance of T' on the diurnal scale is dominated by its NT' component. The largest portion of diurnal T' variance over land is described by variance in

E' (particularly at higher latitudes), while over the ocean it is described by C' . It is therefore important to examine these two components (Figs. 4d–f and 4j–l) to determine the fate of moisture that is in either of these two dominant processes. Over land, moisture that is evaporated goes mostly into an increase in the precipitable water, although at higher latitudes it can be recycled into precipitation. At lower latitudes and in arid regions, evaporation often corresponds to divergent moisture flux. Over the oceans, moisture that converges into a region mostly results in an increase in the precipitable water, although precipitation also may occur outside of the stratocumulus regions. The lack of correspondence between E' and $-C'$ suggests that either a large portion of the divergence occurs outside of the nearly saturated boundary layer, or that there is a significant lag in the response of the ocean surface.

It is also interesting to note several other features in the diurnal variance descriptions. Over tropical Africa, Mexico, and along and just off of many coastlines, diurnal P' corresponds to enhanced C' (Fig. 4c) where local circulations (e.g., land–sea breezes) provide moisture advection into a region during a particular time of day. Over the lush tropical landmasses of the Amazon and Indochina where humidity is consistently very high, all components of the water cycle have comparable variance with a nearly common phase (Figs. 4a–c). Precipitation in these regions draws from evaporation and moisture flux convergence while still drawing down the atmospheric water column. Over high-latitude landmasses, diurnal variations in vapor flux convergence are insignificant (Figs. 4j–l), likely owing to the low moisture content of the cold continental air masses. Similar to RR07a's North American results, only weak regional variation is evident in the behavior of the diurnal water cycle between warm and cold portions of the ocean or high- and low-elevation regions, although meridional and soil moisture variations are apparent.

b. Annual variance description

Normalized covariance maps describing the annual variance of water cycle components are presented in Fig. 5. The most striking aspect of annual variance is the meridional shift in character, which is apparent in nearly all component interactions. Seasons have a larger radiative impact at higher latitudes, and the lower heat capacity of land surfaces also enables larger shifts in temperature than occur over the ocean.

Annual variance in the tropics is dominated by the converging portion of the Hadley circulation, which draws moist lower-tropospheric air into the ITCZ. Both P' and E' have a dynamic Hadley signature, with tropical precipitation dominated by convergence (Fig. 5c)

and subtropical evaporation over the oceans corresponding to the diverging regions underneath the descending portions of the circulation (Fig. 5f).

Many of the annual behaviors occur on land as well as over the oceans. Both C' and P' form the dominant balance throughout the tropics, but also extend their influence over the regions associated with the south and Southeast Asian monsoons. In these areas, large seasonal influxes of moisture correspond to heavy precipitation. A slight seasonal exchange of T' to P' over the low-latitude continents is apparent in Figs. 5b,g, although this is due mostly to the ET' component that dominates the annual tendency variance. The E' also closely corresponds to the ET' variations on this time scale over arid regions, indicating that model evaporation interacts strongly with the model tendencies in these locations, although annual variance for both of these terms is small in comparison to that of precipitation and vapor flux convergence. Annual water cycle variations are largely a balance between the E' , C' , and P' components, reflecting the diminished importance of the tendency terms on this scale.

Seasonal air masses dominate the behavior of the water cycle at higher latitudes. The continental water cycle is dominated by thermodynamic controls due to the low surface heat capacity, with large increases in summertime evaporation accompanied by enhanced precipitation (Fig. 5a) and a slight divergence of water vapor in comparison to strong wintertime dynamical convergence over the continent (Fig. 5k). The E' variance (Figs. 5d–f) is described by a fairly even distribution of moisture to P' and $-C'$ in these areas. Marine air masses precipitate in phase with annual variance in both evaporation and vapor flux convergence (Figs. 5a–c), taking on both a dynamic and thermodynamic exchange.

Large shifts in the water cycle behavior accompany the transition from continental to marine properties as air masses propagate from west to east across the ocean basins. After a long crossing of a relatively dry landmass, continental air masses pick up a lot of evaporated moisture as they move over the Kuroshio or the Gulf Stream (Fig. 5a; note also that a similar pattern exists downwind of the Sahara and over the Somali Current). Until they approach a more saturated lower troposphere, the air masses' water cycle continues to act as if it were still over land, with thermodynamically dominated precipitation that is likely still convective in nature. As the air masses move into the central and eastern ocean basins they begin to act more like the nearly saturated tropical atmosphere as dynamical vapor convergence plays a larger role. At these higher latitudes, however, the dominant precipitation signal (likely

stratiform in nature) is matched by both a large amount of convergent moisture exchange (Fig. 5j) and seasonal evaporative input (Fig. 5d). Upon reaching the western coastlines of continents the saturated air masses converge and dump a large amount of precipitation, particularly where orographic lifting squeezes the atmospheric column in the coastal ranges of North America (Figs. 5a,c).

Other annual variance features are also noteworthy. The narrow equatorial eastern Pacific feature seen in many of the panels is a signature of the double ITCZ that appears over the cold tongue of SSTs in the boreal spring. When this double ITCZ forms, the area on the northern edge of the cold tongue that lies between the two narrow convective bands has enhanced divergence and evaporation, leading to a reduction in precipitation. When the convergence returns after the collapse of this feature, precipitation initiates rapidly. Evaporation does not vary strongly enough to be significant in the vast majority of the moist tropics on these long time scales (Figs. 5d–f), but when it does occur in the stratocumulus regions it acts as a source of atmospheric moisture through its exchange with vapor flux divergence (Fig. 5k).

c. Intraseasonal variance description

The normalized covariances describing the water cycle's intraseasonal variance are provided in Fig. 6. The intraseasonal band is unique in that it is the broadest of the three variance categories examined here and lacks any direct solar forcing. Ranging from ~ 7 to 80 days, this variance category captures propagating synoptic systems, slow Rossby waves, Madden–Julian variability, and tropospheric “rivers” (Newell et al. 1992), among other processes. All of these mechanisms are dynamic in nature, and thus the intraseasonal variance category is dominated by the transients in vapor flux convergence.

The thermodynamic E' term contains the lowest intraseasonal variance, and cannot be significantly described by the other components of the water cycle over the tropics and most land areas (Figs. 6d–f). The lack of low-frequency variance in the tropics was also noted in the annual category, but over land this suggests low thermodynamic sensitivity to passing dynamic disturbances. Difficulties in simulating the clouds that accompany these systems and the soil moisture response to rainfall likely contribute to the insignificant values.

Here C' describes $\sim 100\%$ of the variance in both P' and T' with very little influence from the other components (Figs. 6a–c and 6g–i). For this to occur, the intraseasonal convergence must describe precipitation

and vapor flux convergence independently, as otherwise the variance of the convergent term would exceed either component's variance and normalized covariances of $>100\%$ would result. This suggests that dynamic systems leading to convergence in the intraseasonal band act to either raise the amount of moisture in the atmospheric column or are coincident with precipitation, but rarely do both occur simultaneously. In the intraseasonal band, therefore, there are dual, independent exchange regimes between 1) C' and T' when the convergent region is unsaturated, and 2) C' and P' when the convergent region would otherwise exceed saturation. With much smaller variance, intraseasonal E' covaries with a $-C'$ term that experiences much larger variance (Fig. 6f) due to its interactions with the other two water cycle components. By examining Figs. 6k,l, it becomes clear that evaporation occurs primarily under the first convergent exchange regime, with evaporation helping to speed up the saturation of the atmospheric column.

As the dominant term in the intraseasonal variance category, it is instructive to separate the preferred influence of vapor flux convergence on the other water cycle components. Not surprisingly, the tropical regions that are routinely near saturation show the largest exchange of moisture from convergence to precipitation (Fig. 6j). These regions are also the center of MJO activity. Monsoon precipitation is often manifested in subseasonal systems, and much of the variance in vapor flux convergence in these regions is explained by coincident precipitation. Over arid regions that rarely ever reach saturation, the intraseasonal C' term is explained almost exclusively by T' (Fig. 6l).

The water cycle acts quite consistently between the time scales of the annual and diurnal solar forcing. In fact, the patterns displayed by the intraseasonal band mimic the patterns that are produced when normalized covariances are computed from the components' full (unfiltered) annual time series (not shown). This suggests that the largest percentage of variance is located outside of the narrow bands that define the direct solar forcings, as was observed in RR07b for P' and is also true for C' and T' (E' is dominated by diurnal variance but has a total variance an order of magnitude smaller than C' in most areas). Most of the water cycle's variance is therefore best described by the dynamic vapor flux convergence, which exchanges mainly with precipitation (particularly in the tropics and monsoon regions), although also with increases in the precipitable water tendency (especially in areas of large-scale subsidence) and with evaporation (notably over the stratocumulus regions).

4. Comparison with PERSIANN precipitation

To verify that the results of this study are not overly biased by inadequate convective parameterizations or are too sensitive to the residual definition of the convergent term, the above analysis was also conducted with the R2 precipitation replaced by the Precipitation Estimation from Remotely Sensed Information using Artificial Neural Networks (PERSIANN; see Hsu et al. 1997; Sorooshian et al. 2000) product. The PERSIANN product is among a group of high-resolution precipitation products that were compared to the R2 in RR07b, and uses a suite of remotely sensed products and in situ observations to drive a precipitation estimation algorithm at 3-hourly resolution and $0.25^\circ \times 0.25^\circ$ resolution between 60°N – S latitude. In this study, the PERSIANN precipitation values that fully overlap with any given model grid point were averaged into a single value, approximating the R2's horizontal resolution. In addition, grid points were omitted if more than 20% of the PERSIANN values were missing in any single year from 2002 to 2004, most often due to geosynchronous satellite coverage in the southeast Pacific and over Australia. Ebert et al. (2007) note that high-resolution precipitation products fare better when examining convection and over the oceans, as the interpretation of microwave channels is restricted over land surfaces. RR07b revealed several differences between the R2 and PERSIANN global precipitation fields, most notably the effects of an overactive convective parameterization. To ensure a consistent water cycle balance, the residual vapor flux convergence was calculated over every 3-h forecast period using the model evaporation and precipitable water tendency along with the PERSIANN precipitation rate.

The normalized covariant descriptions of diurnal, annual, and intraseasonal precipitation from the PERSIANN experiment are presented in Fig. 7. Figures 7a–i may be compared to the top (precipitation) rows in Figs. 4–6 that have the corresponding time scale in the R2 model. The descriptions of PERSIANN annual and intraseasonal precipitation are remarkably similar to the R2 precipitation. The intraseasonal (Figs. 7g–i) variance is described even more strongly by the dominant dynamic convergence term. Annual precipitation variance (Figs. 7d–f) displays a strong meridional contrast between the dynamically controlled tropics and an air-mass-driven extratropics that displays the same west–east transition across the ocean basins. Monsoon behavior is very similar, and a signature of a seasonal double ITCZ over the northern edge of the eastern Pacific cold tongue is also apparent. Overall, the PERSIANN experiment's precipitation is explained

by water cycle behaviors that are very similar to those that describe the R2's parameterized precipitation, although several exceptions are noteworthy.

A larger proportion of the globe is insignificant in each of the PERSIANN experiment's variance categories. The PERSIANN product did not capture significant amounts of precipitation over much larger stratocumulus regions in the southeast Atlantic and Pacific Oceans, and of course does not estimate precipitation poleward of 60° latitude. The land surface microwave channel effects on the PERSIANN product also reduce the significance of diurnal and annual precipitation over the mid- and high-latitude continents.

The largest differences between the R2 and PERSIANN experiment water cycles are in the diurnal time scale (Figs. 7a–c). Over the oceans, C' still dominates the description of diurnal P' , although over the tropics there is a larger contribution from E' . However, the C' and T' terms are much more important over the land in the PERSIANN experiment. Both P' and E' are out of phase over much of the tropical land due to a lag between peak early-afternoon evaporation and convective systems that reach their maximum intensity later in the afternoon and early evening.

The nocturnal convective maximum over the Midwest identified by Wallace (1975) has long been an intriguing diurnal phenomenon. The diurnal water cycle behaviors produced by the PERSIANN experiment in this region capture much of the observed variability discussed more extensively in RR07a. Carbone et al. (2002) tracked propagating convective disturbances from their late-afternoon origins over the lee side of the Rocky Mountains to their dissipation in the early morning over the Great Lakes region, replenished by moisture supplied by a nocturnal low-level jet streaming north from the Gulf of Mexico (Higgins et al. 1997b). The evolution of these processes may be inferred from the normalized covariances shown in Figs. 7a–c. Precipitation over the lee side of the Rocky Mountains varies nearly in phase with evaporation (Fig. 7a), indicating an early-afternoon initiation of convection. These phases then grow farther apart as the storms propagate eastward, until P' is $\sim 100\%$ out of phase with E' over the upper Midwest, indicating that convection peaks shortly after midnight. This explanation is also supported by the normalized covariance of T' to P' (Fig. 7b). Over the Rockies, these storms occur when there is normally a positive tendency in precipitable water due to afternoon evaporative input, but as precipitation moves eastward it begins to feed off the supply of moisture already in the atmospheric column at the end of the day. These storms also covary with a large influx of convective moisture (Fig. 7c) that ex-

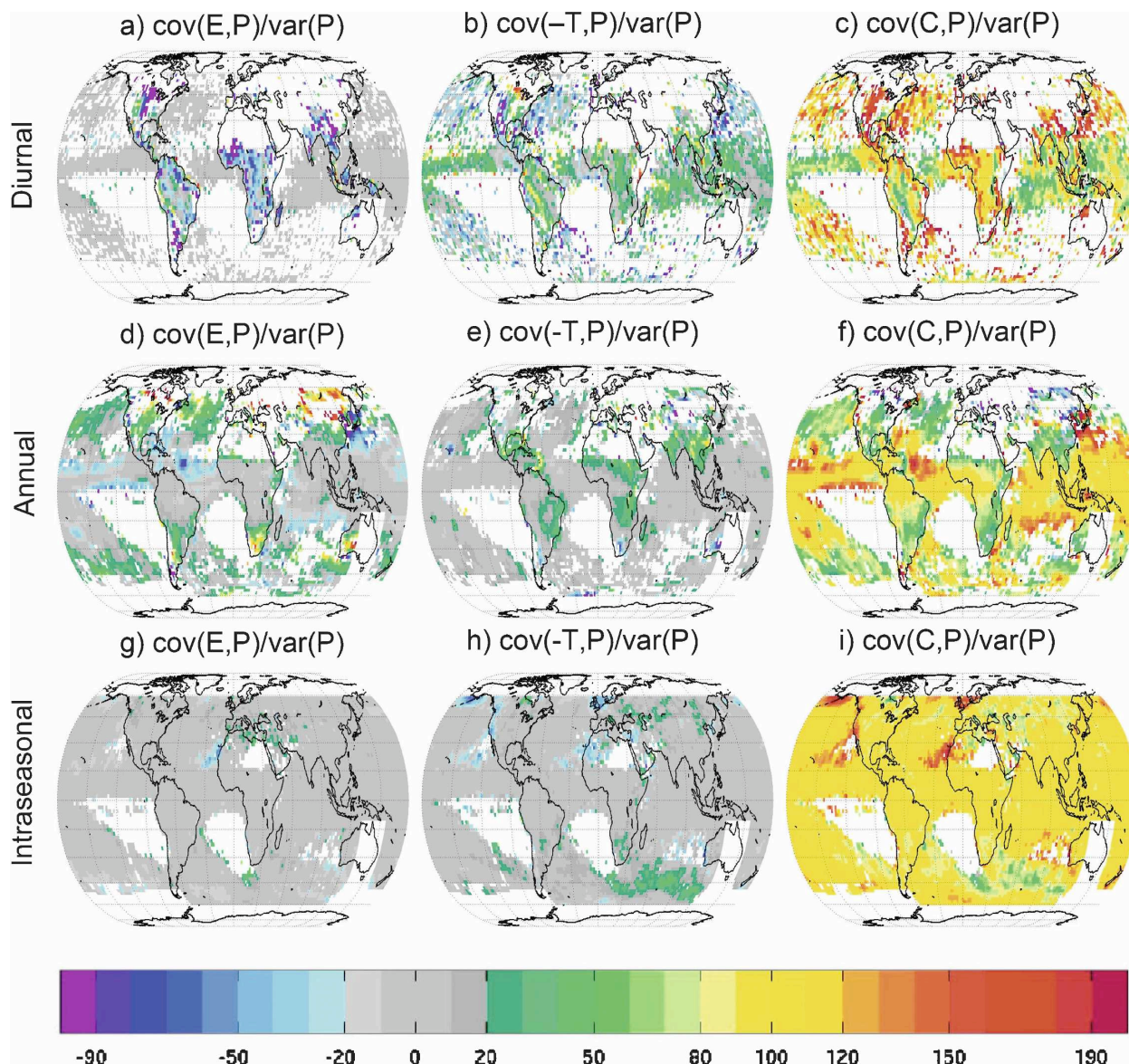


FIG. 7. As in Fig. 4, but for only the precipitation variance description in the PERSIANN experiment. Here each row corresponds to Eq. (9a), but at the time scale indicated on the left: (a)–(c) the diurnal variance, (d)–(f) the annual variance, and (g)–(i) the intraseasonal variance.

tends from the Texas coast into southern Canada and seems to remain in phase with the precipitation bands throughout the entire process (reminiscent of the Great Plains low-level jet; Higgins et al. 1999a).

Additional comparisons were also made with the Experimental Climate Prediction Center's Seasonal Forecast Model reanalysis (SFM; see Kanamitsu et al. 2002a; RR07a; RR07b; not shown). While many of the R2's features discussed above were common to the SFM, the SFM displayed far lower diurnal significance in the description of precipitation's variance over land in the extratropics. Variations in the SFM's annual C'

described virtually all of the ET' variance, suggesting a dynamic tendency interaction as opposed to a largely thermodynamic interaction in the R2. The sensitivities of these normalized covariances to model factors was explored in Ruane and Roads (2008).

5. Conclusions

Examination of the transient balance of the atmospheric water cycle in the NCEP–DOE Reanalysis 2 reveals unique water cycle behaviors at different time scales. The variance of each water cycle process is ex-

plained by its normalized covariance with the other components, which then allows a complete description of the dominant balances and exchanges of the water cycle across the globe.

The diurnal water cycle is characterized by a strong land–sea contrast, with thermodynamic evaporation dominating the continents and dynamic convergence controlling exchanges over the ocean. Some diurnal convective regimes are also fed by moisture convergence that corresponds to diurnal circulation patterns (particularly along tropical coastlines). Although it is largely insignificant at annual and longer time scales, variance in the precipitable water tendency is important over both land and sea.

Annual water cycle behaviors are largely dependent on latitude, with the Hadley circulation dominating the tropics and the extratropics governed by a slow drying and moistening of air masses advected in the westerlies. Monsoon circulations over southern and Southeastern Asia are strongly influenced by long-distance moisture supply that leads to vapor convergence over land. Evaporation in most of the tropics does not vary significantly on this time scale.

Without a direct solar forcing, the intraseasonal variance category is dominated by propagating convergence regions associated with dynamic systems. The exchange of moisture from these systems is dependent on the relative humidity of the convergent environment, with moisture convergence variability corresponding to an increase in the relative humidity in unsaturated regions and precipitation when the environment is saturated. The intraseasonal behaviors also mimic the normalized covariances of the unfiltered time series, suggesting that the largest portion of variance in the water cycle falls outside the direct solar frequencies.

Water cycle behaviors produced describing the variance of precipitation were robust when PERSIANN precipitation replaced the modeled fields (particularly on the intraseasonal and annual time scales), although large portions of the continents become insignificant, due perhaps in part to errors introduced by satellite data over land. The water cycle behaviors that control the intriguing nocturnal precipitation maximum over the Midwest are captured when PERSIANN data are introduced, displaying the signature of afternoon thunderstorms over the Rocky Mountains that are supplied with moisture by a low-level jet as they propagate eastward until the early morning.

As a compliment to RR07b, the results presented here explored the covariant behaviors of unique water cycle features in much greater detail. Still further examinations are possible by focusing on a single time scale and tracking the evolution of individual bandpass-

filtered structures. Preliminary examinations of the surface water cycle and the surface and atmospheric energy cycle using these methods have also proven interesting. The sensitivity of the atmospheric water cycle's transient behaviors to a model's physical parameterizations could shed some light on the relative strengths and weaknesses of the model's parameterization set, as demonstrated in a follow-up work (Ruane and Roads 2008).

Acknowledgments. We are grateful for the support received through NOAA Grant NA17RJ1231 and NASA Grants NNG05GR40G and NNG06GC85G. The views expressed herein are those of the authors and do not necessarily reflect the views of NOAA and NASA. We would also like to thank Masao Kanamitsu for his advice on the R2, Martin Olivera, Jack Ritchie, and Patrick Tripp for technical support, and the three reviewers for their helpful comments.

REFERENCES

- Anderson, B. T., and H. Kanamaru, 2005: The diurnal cycle of the summertime atmospheric hydrologic cycle over the southwestern United States. *J. Hydrometeorol.*, **6**, 219–228.
- , G. Salvucci, A. C. Ruane, J. O. Roads, and M. Kanamitsu, 2008: A new metric for estimating the influence of evaporation on seasonal precipitation rates. *J. Hydrometeorol.*, **9**, 576–588.
- Carbone, R. E., J. D. Tuttle, D. A. Ahijevych, and S. B. Trier, 2002: Inferences of predictability associated with warm season precipitation episodes. *J. Atmos. Sci.*, **59**, 2033–2056.
- Ebert, E. E., J. E. Janowiak, and C. Kidd, 2007: Comparison of near-real-time precipitation estimates from satellite observations and numerical models. *Bull. Amer. Meteor. Soc.*, **88**, 47–64.
- Emery, W. J., and R. E. Thomson, 2004: *Data Analysis Methods in Physical Oceanography*. Elsevier, 638 pp.
- Higgins, R. W., Y. Yao, E. S. Yarosh, J. E. Janowiak, and K. C. Mo, 1997a: Influence of the Great Plains low-level jet on summertime precipitation and moisture transport over the Central United States. *J. Climate*, **10**, 481–507.
- , —, and X. L. Wang, 1997b: Influence of the North American Monsoon System on the U.S. summer precipitation regime. *J. Climate*, **10**, 2600–2622.
- Hsu, K., X. Gao, S. Sorooshian, and H. V. Gupta, 1997: Precipitation estimation from remotely sensed information using artificial neural networks. *J. Appl. Meteor.*, **36**, 1176–1190.
- Kanamitsu, M., W. Ebisuzaki, J. Woollen, S.-K. Yang, J. Hnilo, M. Fiorino, and J. Potter, 2002a: NCEP/DOE AMIP-II Reanalysis (R-2). *Bull. Amer. Meteor. Soc.*, **83**, 1631–1643.
- , and Coauthors, 2002b: NCEP dynamical seasonal forecast system 2000. *Bull. Amer. Meteor. Soc.*, **83**, 1019–1037.
- Koike, T., 2004: The Coordinated Enhanced Observing Period—An initial step for integrated global water cycle observation. *WMO Bull.*, **53** (2), 115–121.
- Lawford, R., and Coauthors, 2006: U.S. contributions to the CEOP. *Bull. Amer. Meteor. Soc.*, **87**, 927–939.
- Lee, M.-I., and Coauthors, 2007: An analysis of the warm season

- diurnal cycle over the continental United States and northern Mexico in general circulation models. *J. Hydrometeor.*, **8**, 344–366.
- Lu, C.-H., M. Kanamitsu, J. O. Roads, W. Ebisuzaki, K. E. Mitchell, and D. Lohmann, 2005: Evaluation of soil moisture in the NCEP–NCAR and NCEP–DOE global reanalyses. *J. Hydrometeor.*, **6**, 391–408.
- Madden, R. A., and P. R. Julian, 1994: Observations of the 40–50-day tropical oscillation—A review. *Mon. Wea. Rev.*, **122**, 814–837.
- Newell, R. E., N. E. Newell, Y. Zhu, and C. Scott, 1992: Tropospheric rivers?—A pilot study. *Geophys. Res. Lett.*, **19**, 2401–2404.
- Pan, H.-L., and L. Mahrt, 1987: Interaction between soil hydrology and boundary layer developments. *Bound.-Layer Meteor.*, **38**, 185–202.
- , and W.-S. Wu, 1995: Implementing a mass flux convection parameterization package for the NMC Medium-Range Forecast Model. NMC Office Note 409, 40 pp. [Available from NCEP/EMC, 5200 Auth Road, Camp Springs, MD 20746.]
- Randall, D. A., Hashvardhan, and D. A. Dazlich, 1991: Diurnal variability of the hydrologic cycle in a general circulation model. *J. Atmos. Sci.*, **48**, 40–62.
- Roads, J., and A. Betts, 2000: NCEP–NCAR and ECMWF reanalysis surface water and energy budgets for the Mississippi River basin. *J. Hydrometeor.*, **1**, 88–94.
- , M. Kanamitsu, and R. Stewart, 2002: CSE water and energy budgets in the NCEP–DOE Reanalysis II. *J. Hydrometeor.*, **3**, 227–248.
- Ruane, A. C., and J. O. Roads, 2007a: The diurnal cycle of water and energy over the continental United States from three reanalyses. *J. Meteor. Soc. Japan*, **85A**, 117–143.
- , and —, 2007b: 6-hour to 1-year variance of five global precipitation sets. *Earth Interactions*, **11**. [Available online at <http://EarthInteractions.org>.]
- , and —, 2008: Diurnal to annual precipitation sensitivity to convective and land surface schemes. *Earth Interactions*, **12**. [Available online at <http://EarthInteractions.org>.]
- Sorooshian, S., K.-L. Hsu, X. Gao, H. V. Gupta, B. Imam, and D. Braithwaite, 2000: Evaluation of PERSIANN system satellite-based estimates of tropical rainfall. *Bull. Amer. Meteor. Soc.*, **81**, 2035–2046.
- Trenberth, K. E., and C. J. Guillemot, 1995: Evaluation of the global atmospheric moisture budget as seen from analyses. *J. Climate*, **8**, 2255–2272.
- , and —, 1998: Evaluation of the atmospheric moisture and hydrologic cycle in the NCEP–NCAR reanalyses. *Climate Dyn.*, **14**, 213–231.
- , A. Dai, R. M. Rasmussen, and D. B. Parsons, 2003: The changing character of precipitation. *Bull. Amer. Meteor. Soc.*, **84**, 1205–1217.
- Wallace, J. M., 1975: Diurnal variations in precipitation and thunderstorm frequency over the conterminous United States. *Mon. Wea. Rev.*, **103**, 406–419.